Physics of Plasmas

Proton acceleration through a charged cavity created by ultraintense laser pulse

Cite as: Phys. Plasmas **26**, 103106 (2019); https://doi.org/10.1063/1.5100094
Submitted: 15 April 2019 . Accepted: 03 October 2019 . Published Online: 16 October 2019

S. Ter-Avetisyan, P. K. Singh, M. H. Cho, A. Andreev, K. F. Kakolee, H. Ahmed, C. Scullion, S. Sharif, P. Hadjisolomou, and M. Borghesi

Physics of Plasmas ARTICLE scitation.org/journal/php

Proton acceleration through a charged cavity created by ultraintense laser pulse

Cite as: Phys. Plasmas **26**, 103106 (2019); doi: 10.1063/1.5100094
Submitted: 15 April 2019 · Accepted: 3 October 2019 ·
Published Online: 16 October 2019

S. Ter-Avetisyan,[1,a)] P. K. Singh,[2] M. H. Cho,[2] A. Andreev,[1] K. F. Kakolee,[2] H. Ahmed,[3] C. Scullion,[3] S. Sharif,[4] P. Hadjisolomou,[3] and M. Borghesi[3]

AFFILIATIONS

[1]ELI-ALPS, Szeged 6728, Hungary
[2]Center for Relativistic Laser Science, Institute of Basic Science, Gwangju 61005, South Korea
[3]School of Mathematics and Physics, The Queen's University of Belfast, Belfast BT7 1NN, United Kingdom
[4]Department of Physics and Photon Science, Gwangju Institute for Science and Technology, Gwangju 61005, South Korea

[a)]sargis.ter-avetisyan@eli-alps.hu

ABSTRACT

The potential of laser-driven ion beam applications is limited by high quality requirements. The excellent "point-source" characteristics of the laser accelerated proton beam in a broad energy range were found by using proton radiographs of a mesh. The "virtual source" of protons, the point where the proton trajectories are converging and form a waist, gradually decreases and moves asymptotically to the target with increasing particles' energy. Computer simulations confirmed that the beam profile at the center is fully conserved, the virtual source of higher energy protons gradually moves closer to the target, and if the particle energy is further increased, the virtual source will be located on the target front surface (for portions above 13 MeV, in this case) with a size comparable to the laser spot size. The laser ponderomotive force pushes the electrons deep into the target creating a bipolar charge structure, i.e., an electron cavity and spike which produces strong accelerating field, realizing a point-size source of accelerated protons. This behavior has not previously been predicted. These results contribute to the development of next generation laser-accelerators suitable for many applications.

I. INTRODUCTION

Recent advances in laser technology have led to extremely intense and high contrast laser pulses which have made it realistic to develop laser-driven ion sources as a reliable, generic technology for applications.[1–3] Laser-driven protons have already opened up new research areas, e.g., proton probing or proton radiography[4,5] by studying the transient plasma fields with unprecedented temporal and spatial resolution, despite the current technology not meeting the required ion beam parameters for many applications. The proton source and beam characteristics are dominated by the ion acceleration scheme and laser pulse parameters.

Ions are created and accelerated in a quasistatic electric field arising from the displacement of hot electrons created by the laser field along the target normal. These ions have maximum energy in the forward direction, the laser propagation direction. In general, charge displacement can occur at the place of laser pulse interaction with the target where electrons, driven mainly by the laser ponderomotive force, electrostatically couple their energy to the ions,[6–8] or, the ions are accelerated through a self-consistent electrostatic field generated by fast electrons escaping in vacuum at the target rear[9]—the target-normal-sheath-acceleration (TNSA).

These processes are not mutual expulsive and the dominance of one mechanism depends on the interaction conditions—the target and laser parameters.[10] However, at oblique laser incidence on an approximately micrometer thick target, the rear side acceleration, i.e., TNSA is the dominant process because inherent laser prepulse or pedestal creates a preplasma at the front of the target and, therefore, only at the rear of the target is it possible to maintain the high gradient of electron temperature and density, and hence, high accelerating field. Ejection of hot electrons to the backside of the target include phenomena such as the fountain effect,[11] electron recirculation through the foil,[12,13] and electromagnetic surface field excitation and propagation[14] which lead to the transverse expansion of the hot electrons along the target surface. Consequently, ion acceleration takes place at the target rear from a much larger area than the laser focal spot, from about hundreds of micrometers area[15] typically with 40°–60° cone angles,[16] known from the TNSA scenario.[17] Because the emission of those protons is laminar, the concept of virtual source was implemented to describe the

proton source/beam properties.[4,5] Assuming the straight line trajectories of protons, the virtual source is the point from where the protons "straight line trajectories" virtually originate. In the TNSA scenario, it was found that the virtual source size is on the order of tens micrometers and located hundreds of micrometers in front of the target.[18]

This paper examines the laser driven proton source and beam characteristics at an intensity of $\sim 10^{20}$ W/cm^2 with a pulse length of 30 fs using mesh proton radiography. Measurements show that having a very high contrast laser pulse (the ratio of peak intensity to prepulse or pedestal intensity) results in the protons, in a broad energy range, accelerated from a very small target region and different energies have similar partial divergence, the divergence of the particles flux from a small volume in the source. The emittance of the beam is preserved in the whole measured spectral range. 2D particle-in-cell (PIC) simulations have revealed the complex dynamic of acceleration processes beyond the experimental limits. It indicates a new mechanism of ion acceleration.

At high intensity and a high contrast laser pulse, the ponderomotive force pushes the hot electrons deep into a target in the form of a moving electron density spike.[19] This produces an electron cavity at the target front with a radius close to the laser focal spot radius r_L with a depth about the nonlinear relativistic skin depth l_s. The latter can be roughly estimated from the balance between the Coulomb force and the ponderomotive force, as the electron spike experiences a strong restoring electrostatic field due to the positive charge left behind.[20,21] The hot electrons propagate along the normal to the surface of this charged cavity with the divergence angle $\theta_d \approx l_s/r_L$.[22,23] Ions, including protons from naturally occurring surface contaminants on the target, are accelerated in the electrostatic field generated between the charge cavity and the electron density spike and this plays an important role in defining the proton source and beam properties.

In the analytical model assuming the adiabatic energy transfer between hot electrons and ions, the temporal evolution of the transverse scale of hot electron charge density profile behind the charge cavity can be predicted, and the distribution of accelerated ions depending on the emission angle can be obtained. Corresponding comparison with PIC simulations has shown good agreement with the suggested approach.

II. EXPERIMENTAL RESULTS

A mesh radiography setup is shown in Fig. 1. The experiments were carried out using a Ti:Sa laser.[24] A 30 fs, p-polarized laser beam along the x-axis was focused onto a 6 μm Aluminum target at 30° of incidence using an f/3 off-axis parabolic mirror. A beam waist of $\sim$4 μm FWHM (contained 30% of 4 J laser energy) resulted in an intensity of $\sim 10^{20}$ W/cm^2. The laser pulse contrast was $<10^{-10}$ several picoseconds before the peak intensity. A 30 μm thick copper mesh with 200 lines per inch was positioned in a distance of $a = 3.7$ mm from the target and imaged by a proton beam on a stack of radio-chromic-films (RCF, type HD-V2) detector located at $b = 26.3$ mm from the mesh (Fig. 1). The proton images of the mesh are shown in Figs. 2 and 3.

A. Radiograph imaging of a mesh

Because of distinct different radiograph images of the mesh obtained with protons having energies above or below $\sim$5 MeV (see Figs. 2 and 3), it is convenient to consider them separately. The images are obtained instantaneously in the same RCF stack detector.

1. "High" energy protons

Typical examples of radiograph imaging of a mesh with protons having energies above $\sim$5 MeV, shown in Fig. 2(a). Images exhibit the proton beams split into small beamlets, and these images have the following features: (i) imaging of a mesh results in clear sharp images of the mesh for each energy of protons. (ii) The spatial profile of proton beamlets at discrete energies has a uniform size distribution and (iii) they are equidistance for all measured energies. However, at the outer part of the beams and at low energies there is measurable symmetric, progressive displacement of beamlets toward to the edges of the mesh but only in a direction perpendicular to the laser polarization (y-axis). This displacement is less noticeable at higher energies. It is also interesting that the detected signal intensity has an ellipse form with a long axis along laser polarization (x-axis). It is worth mentioning that the "size" of the beam seeing on RCF is not the entire size of the proton beam, but only a part of the beam close to the distribution maximum, where the irradiated dose is within the sensitivity of the RCF detector.

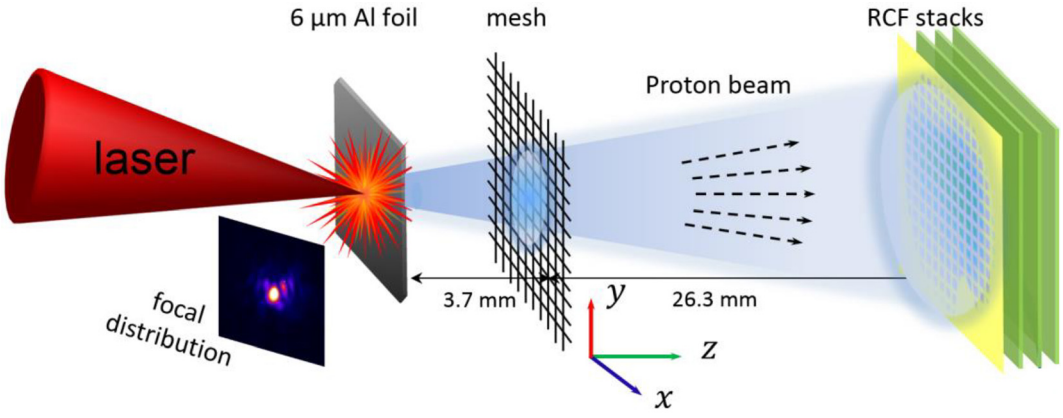

FIG. 1. Experimental setup. Laser accelerated proton imaging of the mesh on a stack of radio-chromic-film (RCF) detector.

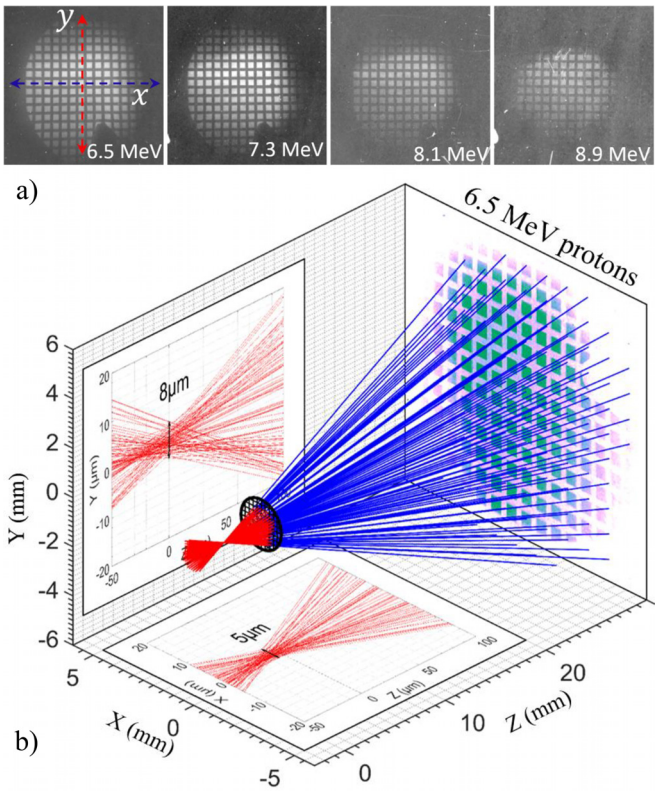

FIG. 2. (a) Mesh images created by protons with energies above 5 MeV, e.g., 6.5, 7.3, 8.1, and 8.9 MeV. (b). Ray-tracing of the mesh image of 6.5 MeV proton beam to the virtual source and the zoomed source projections on (*xz*) and (*yz*) planes. The target between the virtual source and the mesh is not shown in order do not overload the picture.

The same size of all beamlets, observed in the experiment, is possible if a mesh with accurate periodicity is installed perfect-parallel to the detector plane and the beams originate from a point source according to the basic proportionality theorem, Thales theorem. This suggests that the realized imaging geometry is rather accurate and the proton source is like a "point source." Assuming the ballistic propagation of protons and that there are no interactions within the beam, the source properties can be revealed by ray-tracing of the mesh image through a mesh to a point where the traces are converging and form a waist, the virtual source. In Fig. 2(b), a MATLAB code tracks the centroids of all square shapes formed on RCF picture and subsequently creates an image of the mesh with respect to these centroids. The straight line trajectories of protons (ballistic propagation), connecting the mesh to the mesh image, virtually originate from the source with a size of 5–8 μm, as exemplified for 6.5 MeV protons in Fig. 2(b), called virtual source.

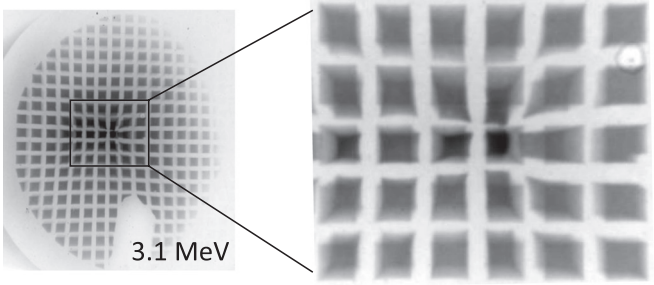

FIG. 3. Typical mesh image created by protons with energies below 5 MeV, e.g., 3.1 MeV on the left. On the right is the zoomed picture of the central part of the mesh.

The virtual source located at the target front only about 20–30 μm far from the target [the target between the virtual source and the mesh in Fig. 2(b) is not shown in order to do not overload the picture] which is a much shorter distance than literature reported values, e.g., in Ref.15, it was estimated several hundreds of micrometer. It can be found from geometry that the protons in a broad energy range are emitted from a region on the target less than 20 μm, which is also much smaller than reported value hundreds of micrometer.[15] Additionally, systematic move of the virtual source toward to the target is observed with increasing the proton energy. This has not been mentioned so far in the literature, to the best of our knowledge.

A qualitative interpretation of these results is that the particles are accelerated from the virtual point source which is located very close to the target and at the same curvature of quasistatic sheath field. Obviously, the curvature of the sheath field rapidly changed in time and space during and after the laser pulse. Therefore, either the whole proton spectrum was generated within the very short time period when there is no significant change in the curvature of the sheath field or the self-similar dynamics of the sheath field has to take place. Similar observations have been made for high energy components of the proton beams in Refs. 25 and 26.

2. "Low" energy protons

Typical example of radiograph imaging of a mesh with protons having energies below 5 MeV, shown in Fig. 3), where a "distorted" image of the mesh appears. The zoomed central part of the left image of Fig. 3 (see right of Fig. 3) shows that indeed the distorted image represents the overlap of the two images: one, is the image of the mesh that has similar properties to the protons above 5 MeV, and the other is the image of the mesh with a relatively less divergent beam. Thus, Fig. 3 is the image of the mesh exposed with two beams with different properties but the same energy.

Ray-tracing of the two overlap images of the mesh shows the existence of two distinct virtual sources (Fig. 4): one source is about 10 μm and located ~30 μm far from the target front, which makes it very similar to the source of high energy protons (above 5 MeV). The other virtual source is almost 4–5 times bigger than the first one and located far from the target front. The latter is most likely the virtual source of protons accelerated by the TNSA, since it has similar characteristics to protons in the TNSA regime.[15,18] Obviously, these sources emit protons with different partial divergences (Fig. 3). Therefore, it is conceivable to conclude that in Fig. 3 the TNSA protons overlap with the protons accelerated from the source whose characteristics differ from TNAS protons, but very similar to the source observed for high energy protons (above 5 MeV).

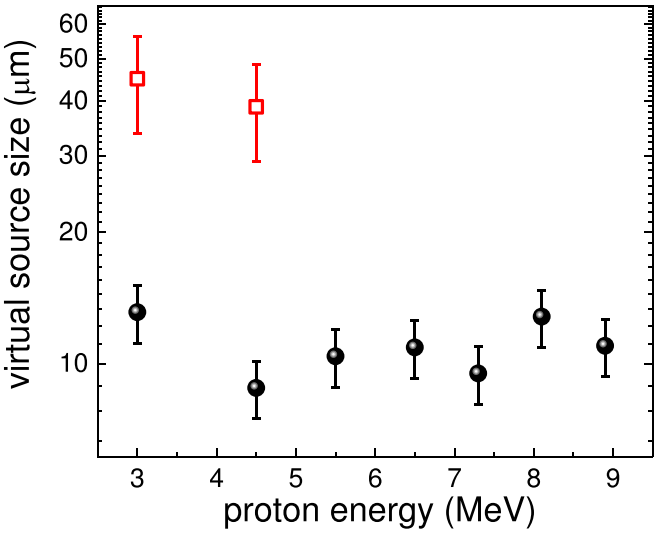

FIG. 4. The measured virtual source size of protons at different energies shown in Figs. 2 and 3. The existence of two distinct different virtual sources is apparent.

B. Data analyses and error estimates

The mesh, as a pepper-pot emittance probe, is used for beam emittance measurements where the main errors are the accuracy of spacing in the mesh, pepper-pot to RCF distance measurement, the detector resolution, and the source size. The detector resolution is defined as $\delta_d = 1.22d(1 - (b/(a+b)))$, where d is the detector pixel size. Using the experimental values $d = 21.2\,\mu$m, $b = 26.3$ mm, and $(a+b) = 30$ mm, the detector resolution will be $\delta_d = 3.2\,\mu$m, smaller than the resolution obtained in the source size estimate ($\sim 10\,\mu$m). Therefore, the anticipated emittance value is limited by the accuracy of source size measurement.

The emittance can be estimated as[27]

$$\varepsilon_{nt} = \beta\gamma\sigma_\theta\sigma_r, \tag{1}$$

where ε_{nt} is the normalized transverse emittance, β is the ratio of proton velocity to speed of light, γ is the beam Lorentz factor, σ_θ is the measured beam RMS divergence, and σ_r is the corresponding RMS virtual source size.

Applying Eq. (1) to the proton beams above 5 MeV, e.g., to the 6.5 MeV protons, the parameters: $\beta = 0.118$, $\gamma = 1.00698$; $\sigma_\theta = 174$ mrad, $\sigma_r = 10\,\mu$m, yield the normalized transverse emittance value $\varepsilon_{nt} \cong 0.065\,\pi$ mm mrad.

Applying Eq. (1) to the proton beams below 5 MeV, e.g., to the 3.1 MeV protons, the parameters: $\beta = 0.081$, $\gamma = 1.003$; $\sigma_\theta = 235$ mrad, $\sigma_r \sim 45\,\mu$m, yield the normalized transverse emittance: $\varepsilon_{nt} \cong 0.273\,(\pm 0.06)\,\pi$ mm mrad.

1. Source size and error estimates

The error in estimating the virtual source size in Fig. 2(b) is due to nonperfect imaging conditions and uncertainties caused by the detector spatial resolution. The analysis of error contributions from different sources is made in estimating the angles of beamlets, e.g., errors in an individual pointing's on mesh image: $\pm 2\,\mu$m, errors in every direction due to mesh spacing, opening size and position: $\pm 1\,\mu$m, and mesh-to-image miscentering, although this error is systematic for an individual setup. The error due to inherent spatial resolution of RCF detectors has additionally degraded to $\pm 5\,\mu$m due to the increased background noise. Therefore, the error in the mathematically reconstructed virtual source size and its projection estimate in Fig. 2(b) is at the limit of the method, $\pm 8\,\mu$m. It should be noted also that because of this limit the measured normalized transverse emittance values for proton beams are an upper estimation.

The G4beamline particle tracer code[28] was used for source size estimates. By placing an object in a path of a divergent proton beam of a given source size and energy ballistically propagating in free space, a projection image of the object can be formed. A 6.5 MeV monoenergetic proton beam of a Gaussian source ($\sigma_x = \sigma_y$ are the width of distribution) consisting of 5×10^6 particles is used to image a mesh with 200 lines per inch on a flat detector. The distances of the mesh and detector from the proton source are 3.7 mm and 30 mm, respectively, similar to the experiments.

A uniform mesh image pattern was generated. The uniformity of mesh resolution across the image plane was examined by the line out of the proton counts for different cells and no difference could be observed. Line out of the mesh edge projections at 3, 5, 10, and 15 μm size of proton source shown in Fig. 5(a) and, in the inset, simulated mesh cell radiographs at 3 and 5 μm size of proton source is shown, as an example. In Fig. 5(a), the line out of measured mesh edge projection gives the best fit, in terms of sharpness of the edges, to the simulated data for a 10 μm source size, which is of the same order as the independent estimate from the ray-tracing code [Fig. 2(b)].

Additionally, in order to verify the effect of possible degradation of spatial resolution of the image due to transparency of the used 30 μm thick mesh to the, e.g., 6.5 MeV protons which have a stopping range of 120 μm, a comparative study was carried out where 6.5 MeV protons were used for projection imaging of 30 μm and 250 μm thick Cu strip, shown in Fig. 5(b). Mesh cell radiographs are shown in the inset. In simulated images for transparent (30 μm) vs opaque (250 μm) copper meshes for 6.5 MeV protons [Fig. 5(b)], the line outs of the cells edges show negligible difference in sharpness, indicating that there is no additional degradation of the image due to the transparency of the mesh.

III. SIMULATIONS AND MODELLING

A. Particle-in-cell simulations

In the 2D PIC simulations, based on the code EPOCH,[29] a p-polarized, 30 fs laser pulse with a Gaussian profile (temporal and spatial) at $\lambda = 0.8\,\mu$m wavelength is focused into a 4 μm spot, having normalized vector potential $a_0 = 7$, under 30° on a 1 μm thick Al^{4+} target with 90 nm H^+ contaminant layers on both sides. These are the parameters used in the experiments except target thickness. A 1 μm target thickness was simulated instead of 6 μm used in the experiments in order to run high-resolution simulation in a reasonable time slot. Also, there is experimental evidence that at the applied intensities here ($\sim 10^{20}$ W/cm^2) the target thickness has almost no influence on maximum proton energy at optimized conditions.[30] In simulations, the initial electron temperature $T_e = 100$ eV. The target is in the xy plane and z is the target normal direction. The simulation mesh has a size of $dx = \lambda/100$ and $dy = \lambda/50$ with 400 particles per cell. The target density was set as 1.74×10^{23} cm^{-3} for H^{1+} and 6.0×10^{22} cm^{-3} for Al^{4+}. The somewhat low density of the hydrogen contaminant layer

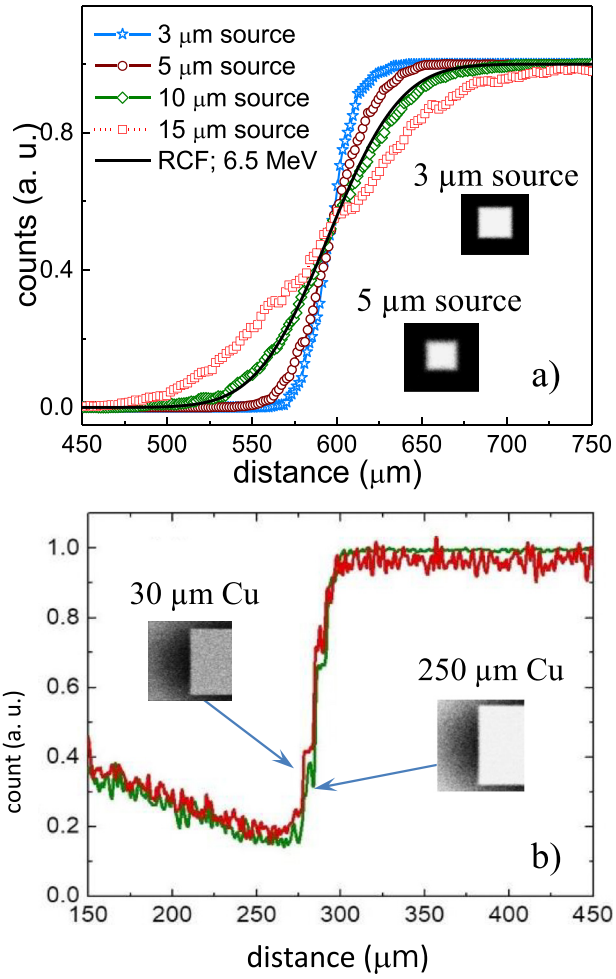

FIG. 5. (a) Line out of the edge projections at 3, 5, 10, and 15 μm size of the proton source simulated by the G4beamline code and measured in the experiment. Inset, mesh cell radiographs at 3 and 5 μm proton source. (b) Line out of the edge projections simulated by G4beamline code for 30 μmand 250 μm thick *Cu* mesh. Mesh cell radiographs shown in the inset.

corresponds to the case of a deposit, unstructured atomic layer of hydrogen on the target surface.

The simulation was mainly focused on reproducing the experimental findings, in particular, on the virtual source and beam properties, rather than on details not yet confirmed by the experiments. 2D PIC simulations have reproduced the spatial characteristics of protons and revealed the details of the source and beam characteristics far beyond the experimental limits. The momentum distribution of protons with energies from 3 MeV up to 15 MeV in phase space at a distance of 50 μm from the target is shown in Fig. 6(a). Here, different energy protons have acquired different transverse momenta which remain unchanged during their further propagation.

The temporal evolution of proton momentum at an early stage of propagation exemplified for 4, 8, and 12 MeV protons is shown in Figs. 6(b) and 6(c). Up to about 400 fs, there is a rapid increase in all particles transverse momentum before it saturates and bunches start to expand linearly after 400 fs due to the particles' time-of-flight (TOF) [Fig. 6(b)]. This somehow contradicts the assumption of ballistic propagation of proton beam made in reconstructing the virtual source of protons. The transverse momentum change of the particles during propagation has direct impact on the virtual source position and size. This finding, however, does not affect the concept of virtual source defined from the linear expansion part of the beam and its importance for applications.

The longitudinal momentum gain for different energy protons takes place differently [Fig. 6(c)]. The high energy protons gain longitudinal momentum for much longer time than the low energy once, e.g., in Fig. 6(c) it is shown that the momentum of 8 MeV and 12 MeV protons increases during ~300 fs and ~400 fs after acceleration, respectively, and 4 MeV protons start to expand linearly by TOF after 100 fs. This changes the longitudinal emittance of the beam and needs to be taken into account at time resolved measurements. The dynamics of electric field profiles in the vicinity of the beams (Fig. 7) shows that the transverse electric field (E_x) at any time step is much weaker as compared to longitudinal field (E_z). Moreover, there is almost no transverse electric field at the center of the beams. Therefore, at the center the beams profile is fully conserved. However, even small transverse electric field at the outer part of the beams results in the progressive displacement of beamlets in a transverse direction as measured in the experiments for the outer region of the mesh images. The particles are gaining additional forward momentum mainly from longitudinal electric field (E_z), as shown in Fig. 6(c).

Figure 8(a) shows the simulated virtual source size and position in front of the target at different proton energies from the particle final momentum values, as it is reconstructed from the experimental mesh images (see Fig. 2). It calculates mean and standard deviation of the particle position until the smallest standard deviation is reached. The virtual source size gradually decreases and moves asymptotically toward to the target surface with increasing particles' energy. The virtual source of protons above 13 MeV is located on the target surface with a size comparable to the laser spot size, which may suggest that the virtual source becomes a real source on the target front. When the rapid increase in particle transverse momentum at early time [<400 fs, Fig. 6(b)] is considered, the virtual source will be even smaller and become located on the target surface at even for lower proton energies (about 10 MeV).

It is interesting to note that the simulated virtual source size of protons with energy less than 5 MeV in Fig. 8(a) corresponds to the virtual source size of TNSA protons (Fig. 3, "distorted image").

The simulated 1D proton image of the mesh at a distance of 4 cm from the target by 4 MeV and 9 MeV proton beams is shown in Fig. 8(b). Despite the simulated large difference in the divergences of chosen proton beams [Fig. 6(a)], the mesh image is similarly reproduced by these two beams. Hence, their partial divergence is the same. The latter agrees well with the experimental findings.

B. Theoretical modeling

The laser ponderomotive force pushes the hot electrons from the focal spot region deep into a target in the form of moving electron density spike.[19] This produces an electron cavity at the target front with a radius close to the laser focal spot radius and the hot electrons propagate along the normal to the surface of this charged cavity. It constitutes the lower limit of the proton source size and the divergence

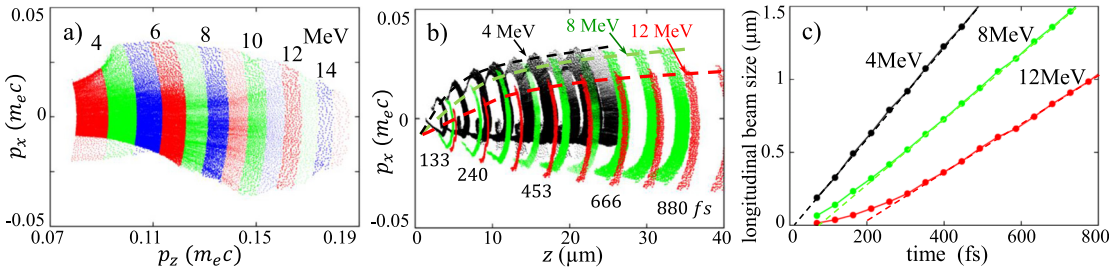

FIG. 6. (a) The momentum distribution of protons for different energies at 50 μm far from the target. (b) The transverse momentum changes and (c) the longitudinal expansion of 4 MeV, 8 MeV, and 12 MeV protons during the propagation.

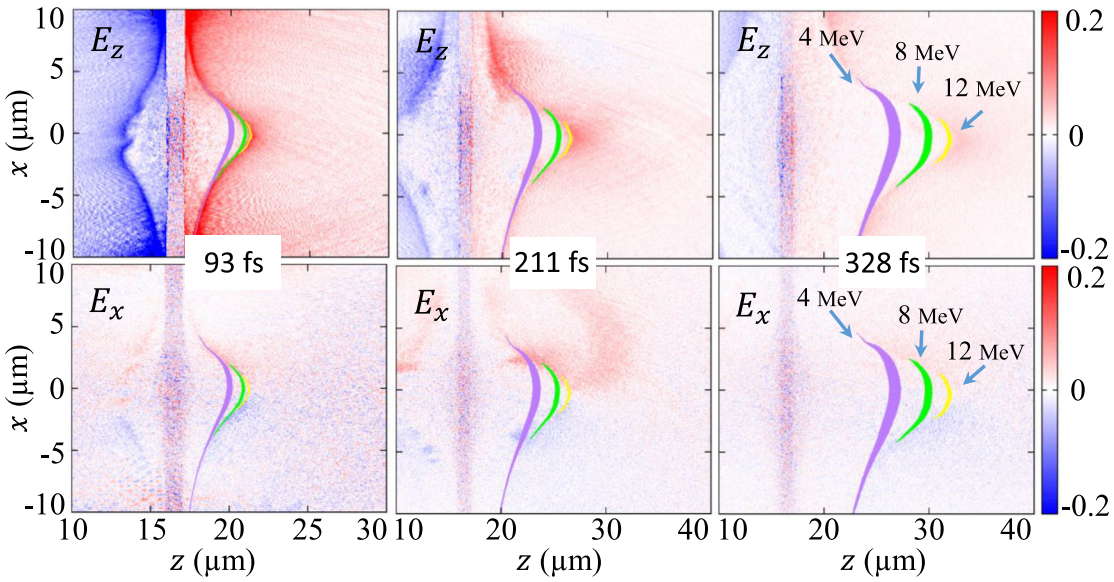

FIG. 7. The temporal evolution of longitudinal (upper row) and transvers (lower row) electric fields created by the electron cloud around 4 MeV, 8 MeV, and 12 MeV proton beams.

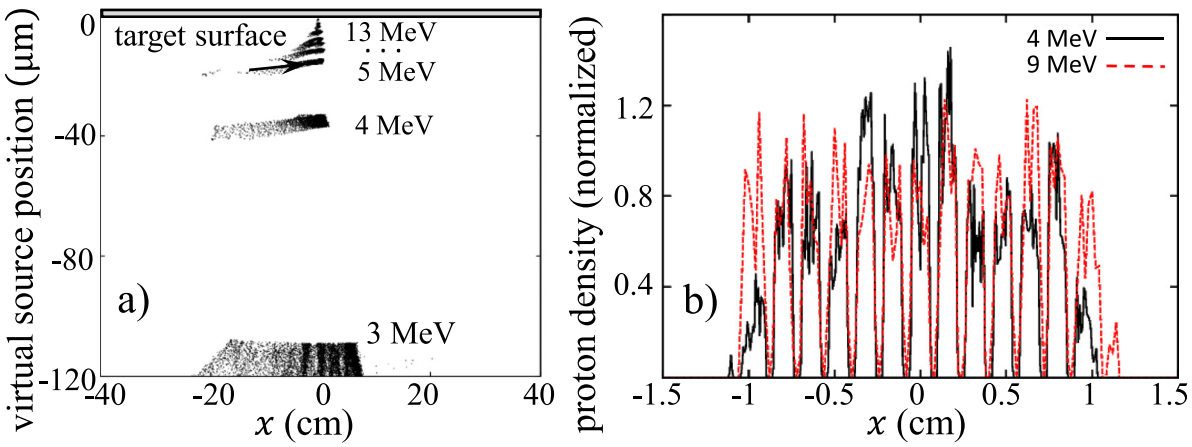

FIG. 8. (a) Simulated virtual source size and its distance from the target for protons with energies from 3 MeV up to 13 MeV is ray-traced from their final momentum value. (b) A simulated 1D image of the mesh, positioned in a distance of 5 mm from the target, created by 4 MeV and 9 MeV protons at 4 cm distance from the target.

of hot electrons. This is in contrast to the longer laser pulses (0.4 and 1 ps) where electrons have rather large divergence[31] and the proton source size is much larger than the laser focal spot size. Adopting the theoretical model[32] based on adiabatic energy transfer between the hot electrons and ions, the hot electron density n_e as a function of the potential φ of charge displacement field behind the charge cavity can be obtained from the adiabatic equation: $\eta_e = 1 + |e|\varphi/2T_{e0}$, $\eta_e = n_e/n_{e0}$. We suppose a temporal evolution of transverse profile of hot electron charge density $\eta(\xi.t)$ results from the normalized transverse scale of the hot electrons at the rear of charge cavity ($l(t) = L(t)/r_D$), which means $\eta(\xi.t) = \eta(\xi.l(t))$. Compared to Ref. 32, the Lorenz distribution was considered: $\varsigma = 3/[1 + (3\xi/l)^2]$, which is close to the simulations, for the longitudinal charge density profile of hot electron density spike behind the charge cavity instead of the delta function used in Ref. 32 for the rear of the target, and the dynamic of electric field was determined. From the Poisson equation, $\eta_e(\xi.\varsigma, l(t))$ is deduced.

The equations of ion motion in the charge separation field can be written as

$$\frac{\partial^2\varsigma}{\partial\tau^2} = \delta\frac{\partial\psi}{\partial\varsigma}, \quad \frac{\partial^2\xi}{\partial\tau^2} = \delta\frac{\partial\psi}{\partial\xi}, \tag{2}$$

where $\delta = m_e/m_i$, $\varsigma = z/r_D$, $\xi = y/r_D$ are the coordinates normalized to the Debye radius of hot electrons $r_D = \sqrt{T_{e0}/4\pi e^2 n_{e0}}$, T_{e0} and n_{e0} their initial temperature and density, $\psi = |e|\varphi/T_{e0}$. The solution gives the angle of ion departure for the given profile of charge distribution

$$\theta(\xi_0) = \frac{\dot{\xi}|_{\tau\to\infty}}{\dot{\varsigma}|_{\tau\to\infty}}. \tag{3}$$

Equation (3) is calculated describing the speed components in terms of field components: transverse and longitudinal with respect to the foil surface, taking into account linear trajectories of ion, according to numerical calculations

$$\theta(\xi_0) = \frac{\partial\xi/\partial\tau|_{\tau\to\infty}}{\partial\varsigma/\partial\tau|_{\tau\to\infty}} \approx \frac{\int_0^\infty E_\eta\big(\xi_o, \nu_i(\xi_o)\tau; l(\tau)\big)d\tau}{\int_0^\infty E_\xi\big(\xi_o, \nu_i(\xi_o)\tau; l(\tau)\big)d\tau}, \tag{4}$$

where ν_i—effective collision frequency, $E_{\eta,\xi}(\xi, \varsigma; l(\tau)) = -2\partial\eta_e(\xi, \varsigma; l(\tau))/\partial(\xi, \eta)$ are the tangential and normal component of the electric field in respect to the foil surface. To calculate the angle at a large distance from the target in the solution of the Poisson equation for $\eta_e(\xi.\varsigma, l(t))$, we substitute the Bessel function with its asymptotic value at $\varsigma > 1$ and calculate this integral by the method of steepest descend. We get: $\theta \approx \sqrt{2}\frac{1}{\eta}\partial\eta/\partial\xi$. The maximum speed accumulated by an ion at the coordinate ξ_o is determined by the maximal value of the nonstationary potential at this point. Figure 9 shows accelerated proton beam divergence at different laser intensities calculated at zero initial speed of the particles at any starting position ξ_o. Here, for comparison, the simulation results from Fig. 6(a) for different laser intensities are plotted which is in good agreement with calculations.

IV. DISCUSSION AND CONCLUSIONS

It has been experimentally demonstrated that energetic protons have been accelerated together in the strong charge-separation field

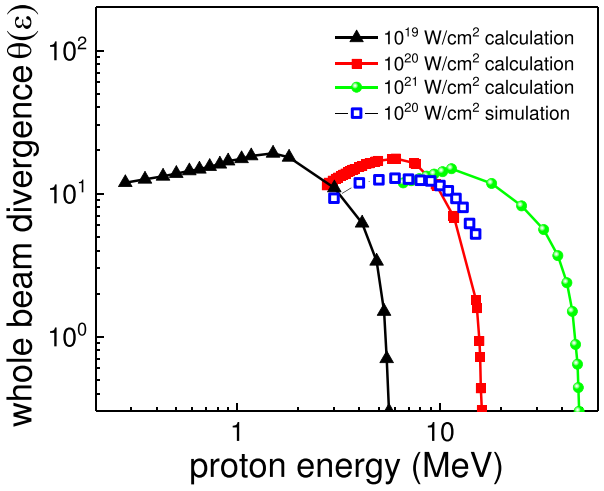

FIG. 9. Polychromatic proton beam divergence calculated at different laser intensities and simulated in Fig. 6(a).

from a "point-size source" with a similar partial divergence in a broad energy range. These findings suggest that a bipolar charge structure, i.e., electron cavity and electron spike is formed from the interaction of high intensity, high contrast, and short laser pulse with a solid target which produces a strong accelerating field where protons are accelerated to high energy. This scenario makes possible forward acceleration of protons from a point-size source for a short time, which leads to a similar partial divergence of beams at different energies. The simulations confirmed that the proton beam profile at the center is fully conserved, because the transverse electric field (E_x) at any time step during the acceleration is much weaker as compared to longitudinal field (E_z) and, moreover, there is almost no transverse electric field at the center of the beams. This is in contrast to protons accelerated in the TNSA regime, which have a relatively larger virtual source size. The cavity–spike accelerated proton normalized emittance was estimated to be $\varepsilon_{nt} \leq 0.065\ \pi$ mm mrad. The experimental results and simulations qualitatively agree with the fact that the virtual source located close to the target front moves toward to the target and the size is gradually decreasing with increasing particles energy [Fig. 8(a)]. There is clear experimental evidence confirmed by simulations that the virtual source of high energy protons gradually moves close to the target and, according to simulations, the virtual source of protons above 13 MeV, in this case, located on the target front surface with a size comparable to the laser spot size. The latest may suggest that the virtual source becomes a real source on the target front, verifying the concept of the limit of the source size. These phenomena have not been previously considered. In contrast, the protons accelerated in the TNSA regime have a relatively larger virtual source and emit protons in the low energy part of the spectra. The applied analytical model based on adiabatic energy transfer between the hot electrons and ions agrees well with simulations on proton beam divergence change with particle energy at these conditions. However, the adiabatic approach might be too "ideal" and some more considerations would be required taking into account the results of further experiments.

The virtual source behavior, its size, and beam properties are crucial for applications dealing with beam quality, beam transport, or

focusing. For instance, in radiography applications, the existence of two sources of protons, and/or moving virtual source may produce an image of the object with features which doesn't correspond to the structure of the object in the object plane. A consequence is that it becomes very complex, and might be impossible to reconstruct the object by image inversion due to the complex features of the source.

ACKNOWLEDGMENTS

This work was performed under the ELI-ALPS Project (No. GINOP-2.3.6-15-2015-00001), supported by EU and co-financed by the European Regional Development fund; T. W. Jeong is acknowledged for the support during the experiments. S. T.-A. thanks V. Yu. Bychenkov for the thoughtful discussions.

REFERENCES

[1]P. K. Patel, A. J. Mackinnon, M. H. Key, T. E. Cowan, M. E. Foord, M. Allen, D. F. Price, H. Ruhl, P. T. Springer, and R. Stephens, Phys. Rev. Lett. **91**, 125004 (2003).
[2]K. W. D. Ledingham, P. McKenna, and R. P. Singhal, Science **300**, 1107 (2003).
[3]E. Lefebvre, E. D'Humières, S. Fritzler, and V. Malka, J. Appl. Phys. **100**, 113308 (2006).
[4]M. Borghesi, A. Schiavi, D. H. Campbell, M. G. Haines, O. Willi, A. J. MacKinnon, L. A. Gizzi, M. Galimberti, R. J. Clarke, and H. Ruhl, Plasma Phys. Controlled Fusion **43**, A267 (2001).
[5]M. Borghesi, D. H. Campbell, A. Schiavi, M. G. Haines, O. Willi, A. J. MacKinnon, P. Patel, L. A. Gizzi, M. Galimberti, R. J. Clarke, F. Pegoraro, H. Ruhl, and S. Bulanov, Phys. Plasmas **9**, 2214 (2002).
[6]J. Denavit, Phys. Rev. Lett. **69**, 3052 (1992).
[7]A. Maksimchuk, S. Gu, K. Flippo, D. Umstadter, and V. Yu. Bychenkov, Phys. Rev. Lett. **84**, 4108 (2000).
[8]O. Shorokhov and A. Pukhov, Laser Part. Beams **22**, 175 (2004).
[9]R. A. Snavely, M. H. Key, S. P. Hatchett, T. E. Cowan, M. Roth, T. W. Phillips, M. A. Stoyer, E. A. Henry, T. C. Sangster, M. S. Singh, S. C. Wilks, A. MacKinnon, A. Offenberger, D. M. Pennington, K. Yasuike, A. B. Langdon, B. F. Lasinski, J. Johnson, M. D. Perry, and E. M. Campbell, Phys. Rev. Lett. **85**, 2945 (2000).
[10]M. Zepf, E. L. Clark, K. Krushelnick, F. N. Beg, C. Escoda, A. E. Dangor, M. I. K. Santala, M. Tatarakis, I. F. Watts, P. A. Norreys, R. J. Clarke, J. R. Davies, M. A. Sinclair, R. D. Edwards, T. J. Goldsack, I. Spencer, and K. W. D. Ledingham, Phys. Plasmas **8**, 2323 (2001).
[11]G. S. Sarkisov, P. Leblanc, V. V. Ivanov, Y. Sentoku, V. Yu. Bychenkov, K. Yates, P. Wiewior, D. Jobe, and R. Spielman, Appl. Phys. Lett. **99**, 131501 (2011).
[12]A. J. Mackinnon, Y. Sentoku, P. K. Patel, D. W. Price, S. Hatchett, M. H. Key, C. Andersen, R. Snavely, and R. R. Freeman, Phys. Rev. Lett. **88**, 215006 (2002).
[13]J. S. Green, N. Booth, R. J. Dance, R. J. Gray, D. A. MacLellan, A. Marshall, P. McKenna, C. D. Murphy, C. P. Ridgers, A. P. L. Robinson, D. Rusby, R. H. H. Scott, and L. Wilson, Sci. Rep. **8**, 4525 (2018).
[14]T. Nakamura, K. Mima, S. Ter-Avetisyan, M. Schnürer, T. Sokollik, P. V. Nickles, and W. Sandner, Phys. Rev. E **77**, 036407 (2008).
[15]M. Borghesi, A. J. Mackinnon, D. H. Campbell, D. G. Hicks, S. Kar, P. K. Patel, D. Price, L. Romagnani, A. Schiavi, and O. Willi, Phys. Rev. Lett. **92**, 055003 (2004).
[16]S. C. Wilks, A. B. Langdon, T. E. Cowan, M. Roth, M. Singh, S. Hatchett, M. H. Key, D. Pennington, A. MacKinnon, and R. A. Snavely, Phys. Plasmas **8**, 542 (2001).
[17]S. Ter-Avetisyan, M. Schnürer, P. V. Nickles, W. Sandner, M. Borghesi, T. Nakamura, and K. Mima, Phys. Plasmas **17**, 063101 (2010).
[18]S. Ter-Avetisyan, M. Schnürer, P. V. Nickles, W. Sandner, T. Nakamura, and K. Mima, Phys. Plasmas **16**, 043108 (2009).
[19]V. Yu. Bychenkov, P. K. Singh, H. Ahmed, K. F. Kakolee, C. Scullion, T. W. Jeong, P. Hadjisolomou, A. Alejo, S. Kar, M. Borghesi, and S. Ter-Avetisyan, Phys. Plasmas **24**, 010704 (2017).
[20]S. C. Wilks, W. L. Kruer, M. Tabak, and A. B. Langdon, Phys. Rev. Lett. **69**, 1383 (1992).
[21]S. X. Luan, W. Yu, M. Y. Yu, G. J. Ma, Q. J. Zhang, Z. M. Sheng, and M. Murakami, Phys. Plasmas **18**, 042701 (2011).
[22]A. A. Andreev, R. Sonobe, S. Kawata, S. Miyazaki, K. Sakai, K. Miyauchi, T. Kikuchi, K. Platonov, and K. Nemoto, Plasma Phys. Controlled Fusion **48**, 1605 (2006).
[23]V. M. Ovchinnikov, D. W. Schumacher, M. McMahon, E. A. Chowdhury, C. D. Chen, A. Morace, and R. R. Freeman, Phys. Rev. Lett. **110**, 065007 (2013).
[24]T. J. Yu, S. K. Lee, J. H. Sung, J. W. Yoon, T. M. Jeong, and J. Lee, Opt. Express **20**, 10807 (2012).
[25]J. Schreiber, S. Ter-Avetisyan, E. Risse, M. P. Kalachnikov, P. V. Nickles, W. Sandner, U. Schramm, D. Habs, J. Witte, and M. Schnürer, Phys. Plasmas **13**, 033111 (2006).
[26]S. Ter-Avetisyan, L. Romagnani, M. Borghesi, M. Schnürer, and P. V. Nickles, Nucl. Instrum. Methods Phys. Res., Sect. A **623**, 709 (2010).
[27]G. Golovin, S. Banerjee, C. Liu, S. Chen, J. Zhang, B. Zhao, P. Zhang, M. Veale, M. Wilson, P. Seller, and D. Umstadter, Sci. Rep. **6**, 24622 (2016).
[28]See http://www.muonsinternal.com/muons3/G4beamline for G4beamline particle tracer code.
[29]T. D. Arber, K. Bennett, C. S. Brady, A. Lawrence-Douglas, M. G. Ramsay, N. J. Sircombe, P. Gillies, R. G. Evans, H. Schmitz, and A. R. Bell, Plasma Phys. Controlled Fusion **57**, 113001 (2015).
[30]S. Ter-Avetisyan, P. K. Singh, K. F. Kakolee, H. Ahmed, T. W. Jeong, C. Scullion, P. Hadjisolomou, M. Borghesi, and V. Yu. Bychenkov, Nucl. Instrum. Methods Phys. Res., Sect. A **909**, 156 (2018).
[31]R. B. Stephens, R. A. Snavely, Y. Aglitskiy, F. Amiranoff, C. Andersen, D. Batani, S. D. Baton, T. Cowan, R. R. Freeman, T. Hall, S. P. Hatchett, J. M. Hill, M. H. Key, J. A. King, J. A. Koch, M. Koenig, A. J. MacKinnon, K. L. Lancaster, E. Martinolli, P. Norreys, E. Perelli-Cippo, M. Rabec Le Gloahec, C. Rousseaux, J. J. Santos, and F. Scianitti, Phys. Rev. E **69**, 066414 (2004).
[32]A. Andreev, T. Ceccotti, A. Levy, K. Platonov, and Ph. Martin, New J. Phys. **12**, 045007 (2010).